

Figure 4.5: Phonon density of states for austenitic stainless steel Fe-18Ni-12Cr-2Mo, (●) experimental data, (—) multiphonon contribution and (△) DOS after multiphonon correction, $\langle u_{\alpha}^2 \rangle = 0.00403 \text{ \AA}^2$.

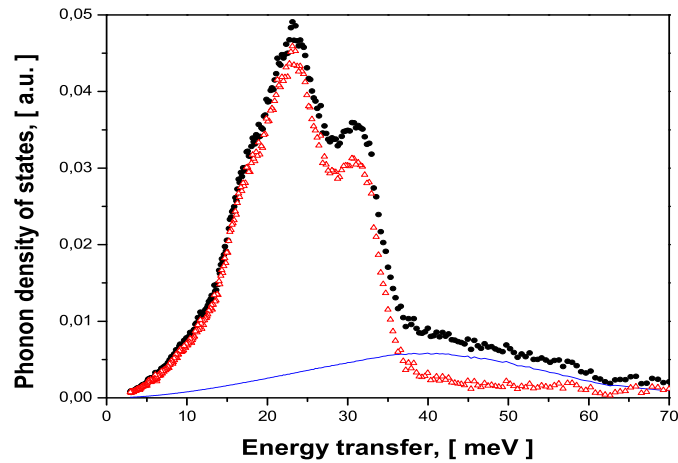


Figure 4.6: Phonon density of states for austenitic stainless steel Fe-18Ni-10Cr, (●) experimental data, (—) multiphonon contribution and (△) DOS after multiphonon correction, $\langle u_{\alpha}^2 \rangle = 0.00392 \text{ \AA}^2$.

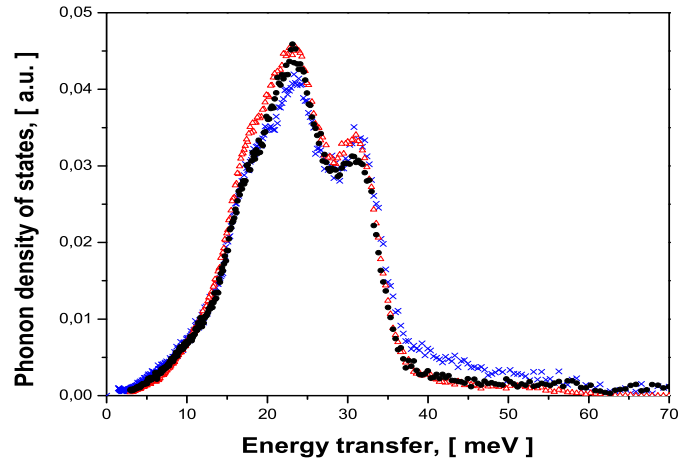


Figure 4.7: Phonon density of states for austenitic stainless steel (\bullet) Fe-18Ni-12Cr-2Mo, (\triangle) Fe-18Ni-16Cr-10Mn and Fe-18Ni-10Cr (\times) after multiphonon correction.

After the subtraction of the multiphonon contribution (fig. 4.4,4.5,4.6) the data were corrected by the resolution function of the spectrometer to enable a comparison with model calculations. For the resolution function a gaussian distribution with a FWHM of 2 meV was used. Data for resolution function including FWHM are obtained from a vanadium scan.

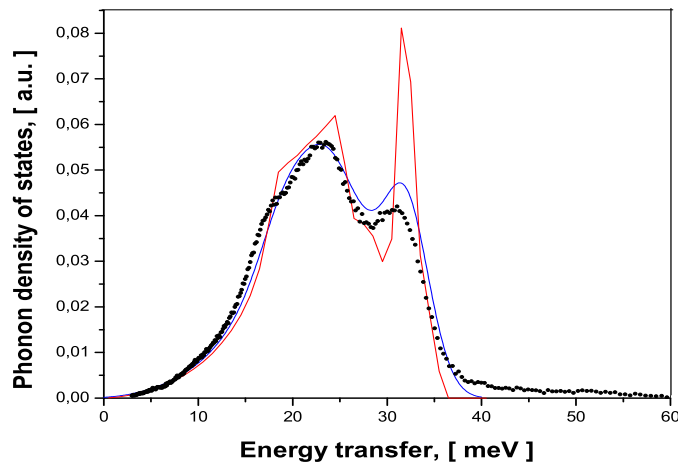


Figure 4.8: Phonon density of states, (\bullet) experimental data for austenitic stainless steels Fe-18Cr-16Ni-10Mn, ($-$) comparison with simulated data using the Born-von-Karman model, generalized force with 2 neighbouring shells and ($-$) with the same model using contributions from the resolution function.

The phonon density of states in Fe-18Cr-16Ni-10Mn, Fe-18Cr-12Ni-2Mn and Fe-18Cr-10Mn show a great similarity (Fig. 4.7). The derived DOS show a significant difference to the experimental data, but when the resolution function was introduced the discrepancy is significantly reduced (fig. 4.8). This behaviour is especially pronounced for the longitudinal mode of vibration (fig. 4.8).

4.4 Thermal properties

From both the INS data on single crystals as well as on polycrystalline samples values were obtained for the elastic constants and moduli, respectively. On the other hand thermal properties are much more sensitive to the peak in the DOS than to the low energy limits. Using the relation for the Debye temperature from [Beskrovni 1999] a value of Debye temperature $\Theta_D=416$ K was obtained. The values for the Debye temperature were in good agreement with experimental data for similar Fe-Cr-Ni alloys [Beskrovni 1999](eq. 2.859 and with pure metals Fe, Cr, Ni, Mo. From the DOS the specific heat capacity c_V (eq. 2.80), the internal energy U (eq. 2.78), the mean squared displacement $\langle \Delta x^2 \rangle$ (eq. 3.19) and Debye temperature $\Theta_D(T)$ (eq. 2.81) can be obtained (table 4.2)

Table 4.2: Debye temperature of some transition metals and some of their alloys (austenitic stainless steels).

| system | Debye temperature Θ_D [K] |
|---------------------------------------------------------------------------|----------------------------------|
| Fe-Cr-Ni alloys | 386-396 [Beskrovni 1999] |
| Fe | 420 [Ashcroft 1976] |
| Ni | 375 [Ashcroft 1976] |
| Cr | 460 [Ashcroft 1976] |
| Mn | 400 [Ashcroft 1976] |
| Mo | 380 [Ashcroft 1976] |
| Fe-18Cr-12Ni-2Mo | 406 [this study] |
| Fe-18Cr-16Ni-10Mn | 410 [this study] |
| generalised force model 2 nd | 418 [this study] |
| generalised force model 2 nd with electron gas contribution | 414 [this study] |

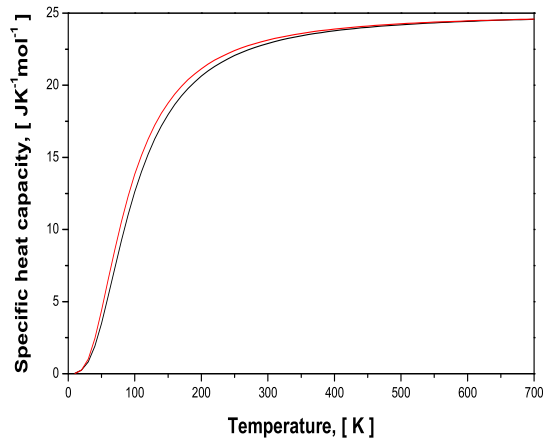


Figure 4.9: Specific heat capacity c_V (—) calculated from DOS for Fe-18Cr-12Ni-2Mo and (—) from the Debye model for Debye temperature $\Theta_D = 406$ K.

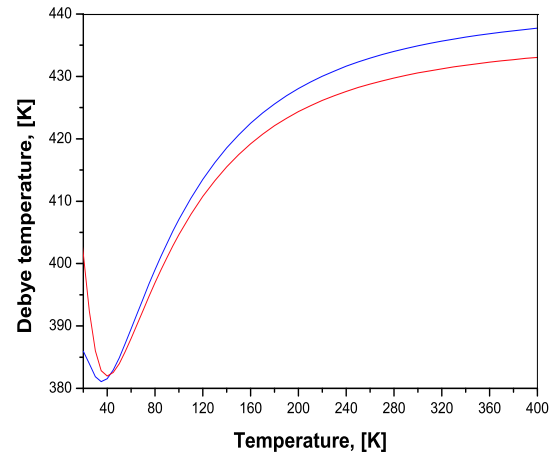


Figure 4.10: Debye temperature as a function of temperature for the austenitic stainless steels (—) Fe-18Cr-16Ni-10Mn and (—) Fe-18Cr-12Ni-2Mo.

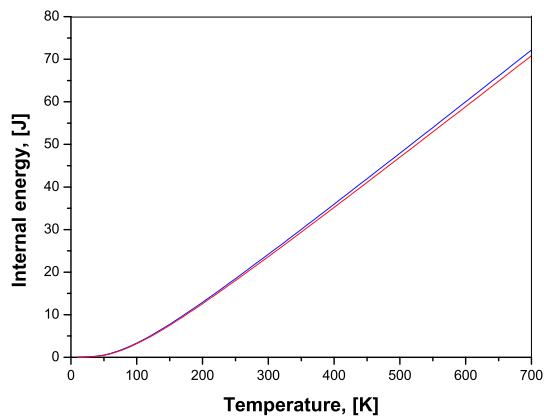


Figure 4.11: Internal energy U (—) calculated from experimental data for Fe-18Cr-12Ni-2Mo and (—) from the Debye model for Debye temperature $\Theta_D = 406$ K.

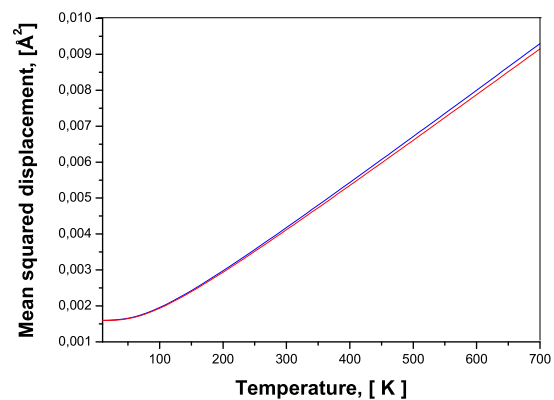


Figure 4.12: Mean squared displacement $\langle \Delta x^2 \rangle$ calculated from experimental data (—) for Fe-18Cr-12Ni-2Mo and (—) from the Debye model for Debye temperature $\Theta_D = 406$ K.

A mean squared $\langle \Delta x^2 \rangle = 0.00412 \text{ \AA}^2$ was obtained, which corresponds to $B_{iso} = 0.325 \text{ \AA}^2$ from the Debye model values for a given Debye temperature $\Theta_D = 416$ K. Similar data was also obtained directly from the phonon density of states in the austenitic stainless

steels Fe-18Cr-12Ni-2Mo, Fe-18Cr-16Ni-10Mn and Fe-18Cr-10Ni. These values showed good agreement with other diffraction studies from which values of $B_{iso}=0.3-0.4 \text{ \AA}^2$ were obtained.

4.5 Conclusion

The phonon dispersion curves for the steels Fe-18Cr-12Ni-2Mo and Fe-18Cr-16Ni-10Mn are very similar (fig. 4.3). The Born-von-Karman model together with the generalized force matrices (5 neighbouring shells) fits well to the experimental data (Fig. 4.3). Using the Born-von Karman model with only two neighbouring shells and introducing the electron gas contribution instead, a significant improvement of the fit can be achieved.(Fig. 4.2). With this approach a satisfactory fitting with only few fitting parameters was obtained. From the force constants and applying the Born-von-Karman model the elastic constants and moduli were obtained (fig. 4.1). The obtained values show good agreement with ultrasonic measurements on different Fe-Cr-Ni-Mn systems. For comparison, also ultrasonic studies in the system Fe-18Cr-12Ni-2Mo [Ledbetter 1981] were used. In the case of Fe-18Cr-16Ni-10Mn [Kim 1994] empirical relations as well as data of ultrasonic studies on polycrystalline samples were used. To obtain really accurate data for the elastic constants and moduli, it is necessary to perform ultrasonic studies on single crystal samples.

Densities of states for austenitic stainless steels Fe-18Cr-12Ni-2Mo, Fe-18Cr-16Ni-10Mn and Fe-18Cr-10Ni are extremely similar (fig. 4.7). Modelling of DOS based on force constants obtained from dispersion curves, show a significant discrepancy (fig. 4.8). Instrument resolution function smears the peak profiles, which have been derived from dispersion curves. When the contribution of the resolution function is also included, it significantly reduces the difference between the experimental and the modelled data. The differences between different steels are much smaller than those between experiment and modelling. From the DOS the thermal properties were obtained Debye temperature $\Theta(T)$ (fig. 4.10), internal energy (fig. 4.11) and specific heat capacity (fig. 4.9). The agreement for the Debye temperature obtained from a low energy fit of the DOS and the values calculated from the Einstein-Madelung-Sutherland relation (eq. 2.85) is pretty good. These values are similar to those reported by [Beskrovni 1999] for other Fe-Cr-Ni-Mn systems based on inelastic scattering studies (table 4.2). It is observed, that Θ_∞ is slightly higher for the Fe-18Cr-10Ni system, this could be connected to a lower intensity of the longitudinal modes. The heat capacities of all 3 samples show great similarity to each other and to the calculations based on the Debye model. Beside this, calculations of the mean squared displacement based on the Debye model (fig. 4.12) and directly derived from the density of states are plausible to each other. This result also confirms the correctness of the calculation procedure.

Chapter 5

Lattice dynamics of hydrogenated austenitic stainless steels

The results of diffraction are used as the input for performing modelling. Especially the distribution of hydrogen and the lattice parameters are important. From this data metal-hydrogen distances were obtained.

5.1 Diffraction study

5.1.1 Experiment

The hydrogenations have been carried out in the Institute of Solid State Physics of the Russian Academy of Sciences in Chernogolovka (Moscow district). The samples consisted of stacks of 3 - 6 discs, each of them has 8 mm in diameter and 0.25 mm thickness. The hydrogen loadings were performed in a high pressure cell at 350 °C for 24 h. Various pressures - up to 7 GPa - were applied in order to obtain several hydrogen concentrations up to $H/Me \approx 1$. In addition to hydrogenations, also deuterium chargings have been carried out. After the hydrogen chargings the samples were cooled down to 100 K and stored at liquid nitrogen to prevent the outgassing of hydrogen.

In the case of samples with low hydrogen content ($H/Me \ll 0.1$) loading pressure are 10-20 MPa. Samples are hydrogenated and deuterated at the Institute for solid state physics, University of Darmstadt.

Neutron diffraction

The neutron diffraction experiments have been carried out⁴ at diffractometer E9 at the Hahn-Meitner-Institute in Berlin, BT1 at the National Institute of Standards and Technology (NIST) in Gaithersburg as well as D1B in Institute Laue-Langevin (ILL) in Grenoble. Diffraction experiment was performed at low temperature (80 K) to prevent outgassing.

⁴experiments and Rietveld refinements were performed by Markus Hölzel

At powder diffractometer D1B Fe-25Cr-20Ni and Fe-18Cr-10Ni were characterised. In the case of Fe-18Cr-10Ni with low hydrogen content, neutron diffraction was performed at triple axis spectrometer E1(HMI). Neutron with wave length $\lambda=2.431 \text{ \AA}$, were used with graphite(002) monochromator and $\lambda=1.231 \text{ \AA}$, with Ge(311) monochromator. Highly hydrogenated samples are investigated on the diffractometer E9(HMI), with Ge(711) monochromator which allow wavelength of $\lambda=1.3078 \text{ \AA}$. At the powder diffractometer BT1 Fe-18Cr-10Ni with loading pressures between 3-7 GPa on 80 K were investigated. The monochromator is Cu(311) and $\lambda=1.5398 \text{ \AA}$.

X-ray diffraction

X-ray diffraction was performed⁵ in samples with very low hydrogen content at room temperature with powder diffractometer D500 for the checking of phase composition.

The X-ray investigations on samples with high hydrogen content powder diffractometer STOE STADI P was used. In this experiment as source was used cathode tube with Mo- K_{α_1} and Cu- K_{α} in the transmission mode. Samples were cooled with gas flow nitrogen.

5.1.2 Result

Diffraction data were analysed with software package [Fullprof 2002].

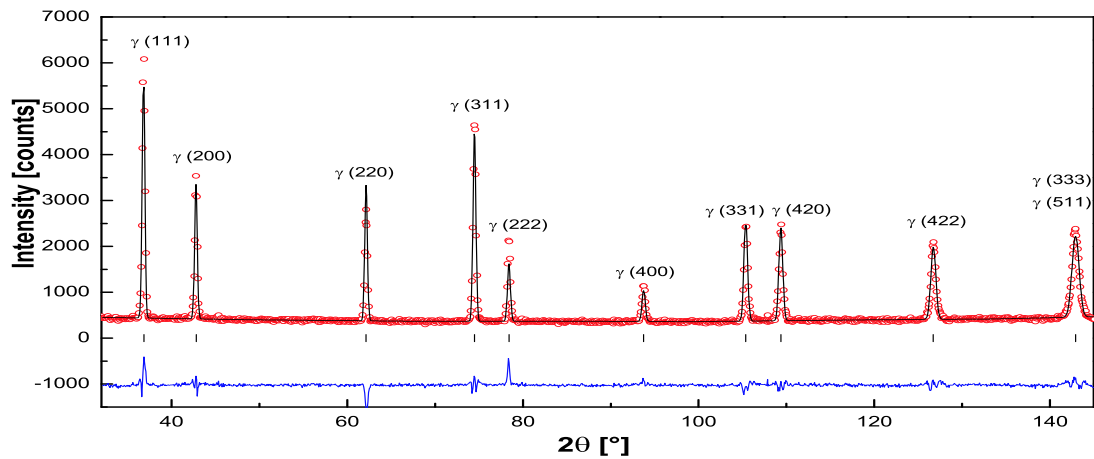


Figure 5.1: The Rietveld refinement of the powder neutron diffraction data of Fe-25Cr-20Ni(diffractometer E9, $\lambda=1.30747 \text{ \AA}$).

⁵experiments and Rietveld refinements were performed by Markus Hölzel

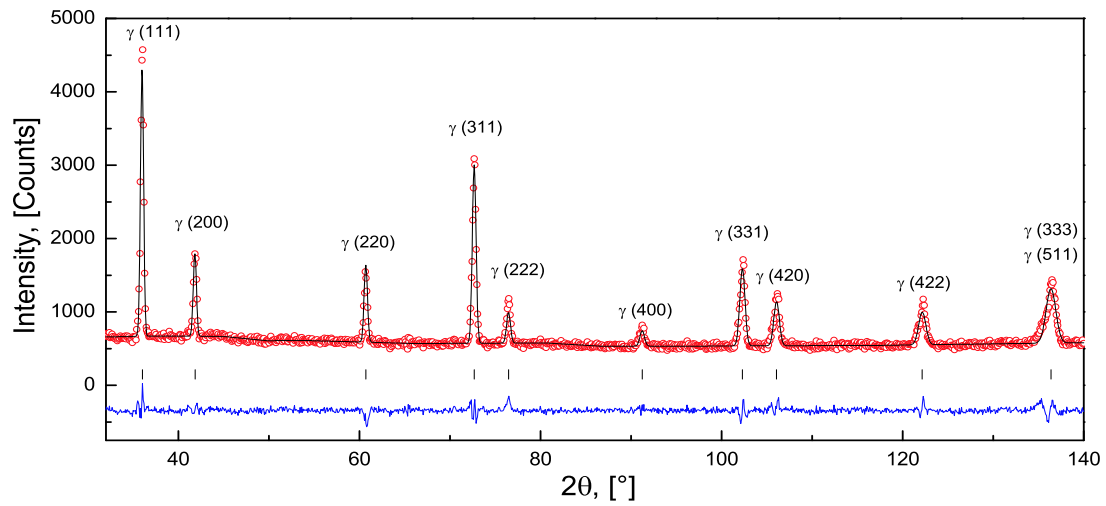


Figure 5.2: The Rietveld refinement of the powder neutron diffraction data of hydrogenated Fe-25Cr-20Ni with loading pressure of 2.3 GPa (diffractometer E9, $\lambda=1.30747 \text{ \AA}$).

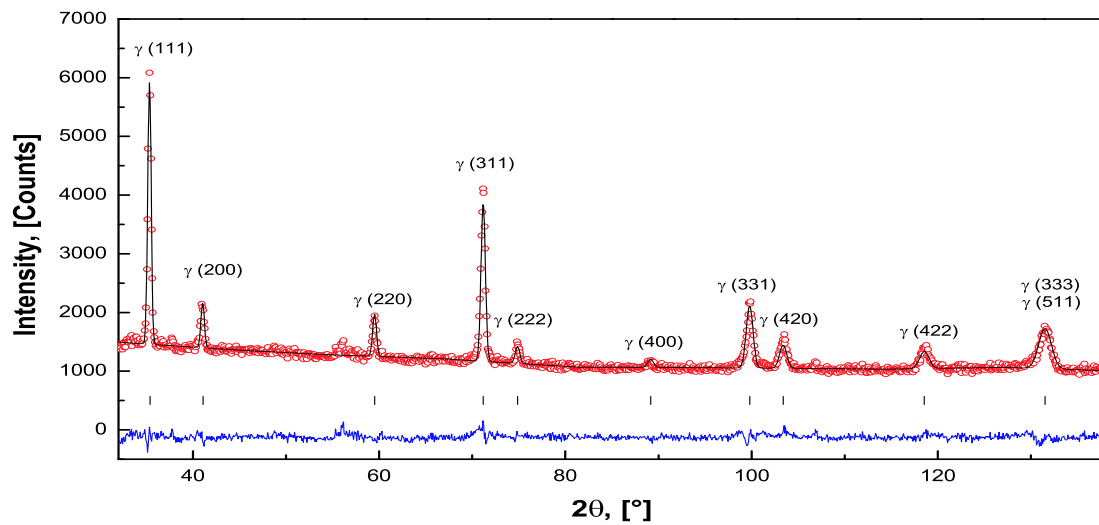


Figure 5.3: The Rietveld refinement of the powder neutron diffraction data of hydrogenated Fe-25Cr-20Ni with loading pressure of 3.0 GPa (diffractometer E9, $\lambda=1.30747 \text{ \AA}$).

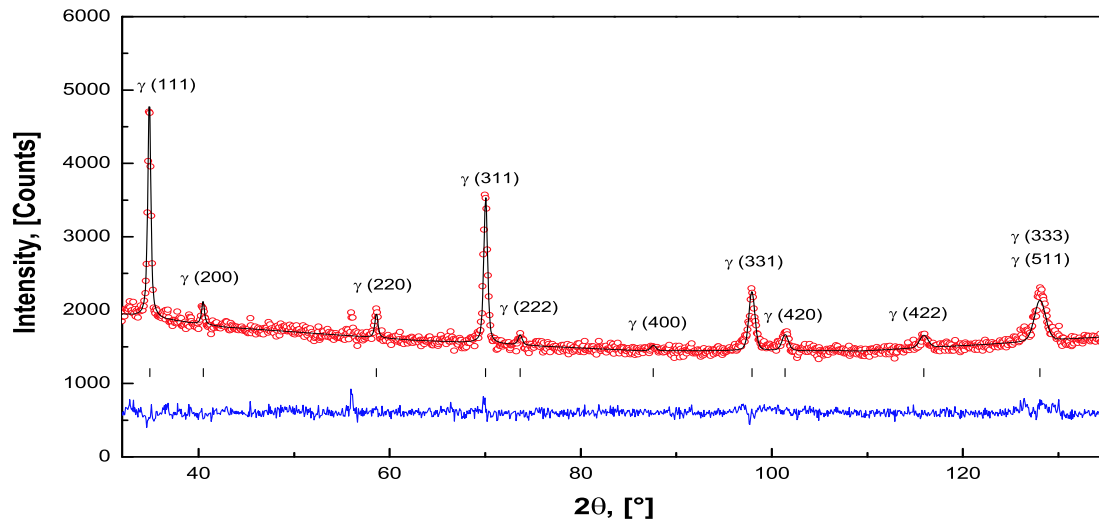


Figure 5.4: The Rietveld refinement of the powder neutron diffraction data of hydrogenated Fe-25Cr-20Ni with loading pressure of 7.0 GPa (diffractometer E9, $\lambda=1.30747 \text{ \AA}$).

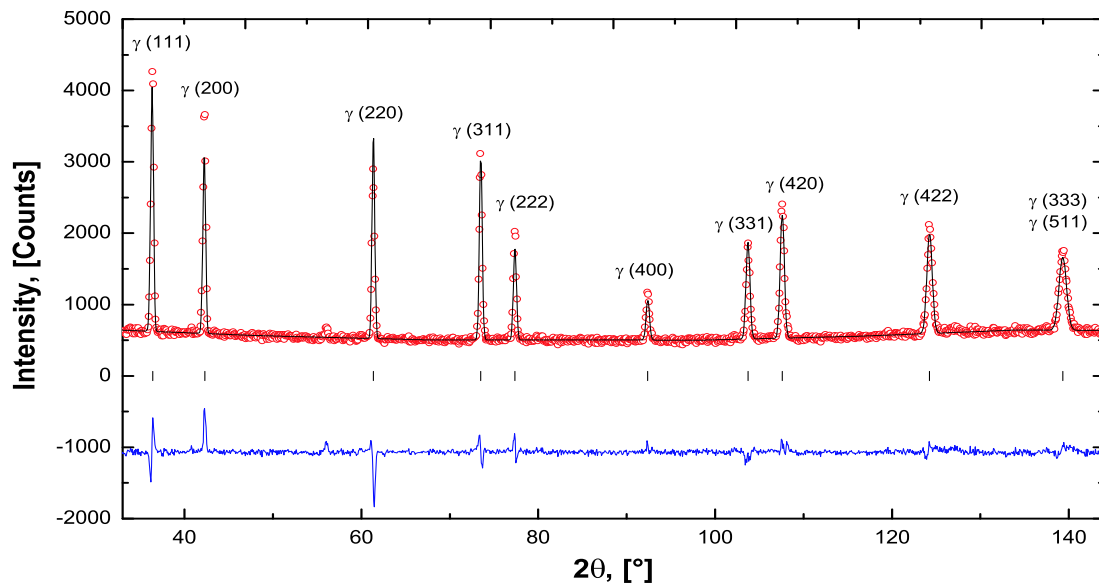


Figure 5.5: The Rietveld refinement of the powder neutron diffraction data of deuterated Fe-25Cr-20Ni with loading pressure of 7.0 GPa (diffractometer E9, $\lambda=1.30747 \text{ \AA}$).

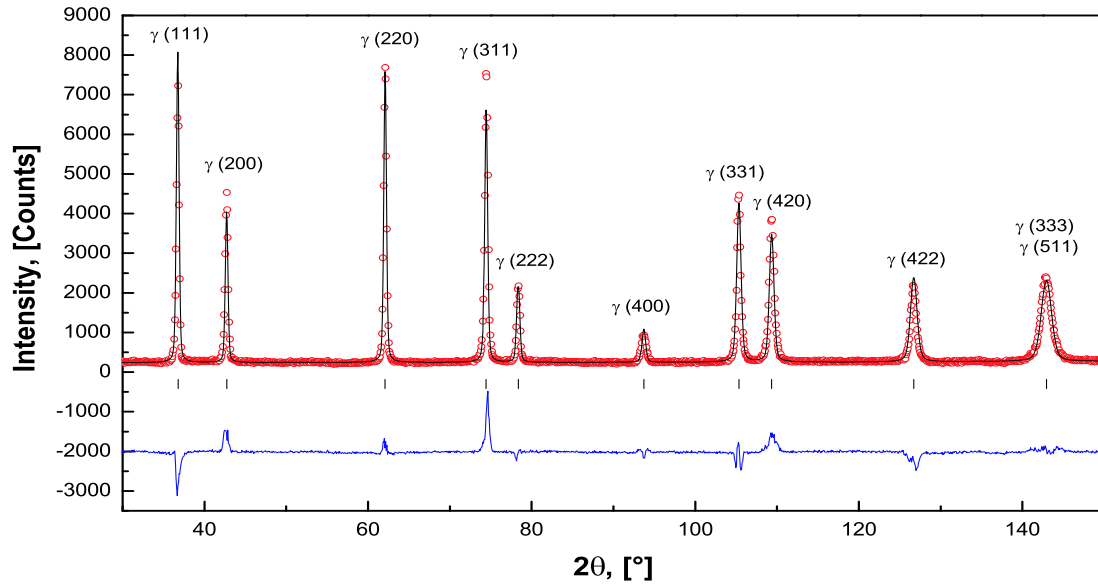


Figure 5.6: The Rietveld refinement of the powder neutron diffraction data of Fe-25Cr-20Ni with loading pressure of 4.0 GPa (diffractometer E9, $\lambda=1.30747 \text{ \AA}$).

Table 5.1: Result of Rietveld refinement for austenitic stainless steel Fe-25Cr-20Ni

| hydrogenation pressure [GPa] | weight frac. of phases | lattice constant (at 80 K) | H(D) occ. in octahed. sites | $B_{iso}(H)$ (\AA^2) |
|------------------------------|------------------------|----------------------------|-----------------------------|---------------------------------|
| uncharged | 100 % $Fm\bar{3}m$ | $a = 3.5826(1)$ | - | - |
| 2.3 | 100 % $Fm\bar{3}m$ | $a = 3.6586(1)$ | 35(2) % | 1.35 |
| 3.0 | 100 % $Fm\bar{3}m$ | $a = 3.7261(2)$ | 66(3) % | 1.44 |
| 7.0 | 100 % $Fm\bar{3}m$ | $a = 3.7798(2)$ | 94(5) % | 1.48 |
| Deuteration | 100 % $Fm\bar{3}m$ | $a = 3.6236(1)$ | 13(1) % | 0.96 |
| 4.0 without H | 100 % $Fm\bar{3}m$ | $a = 3.5824(2)$ | - | - |

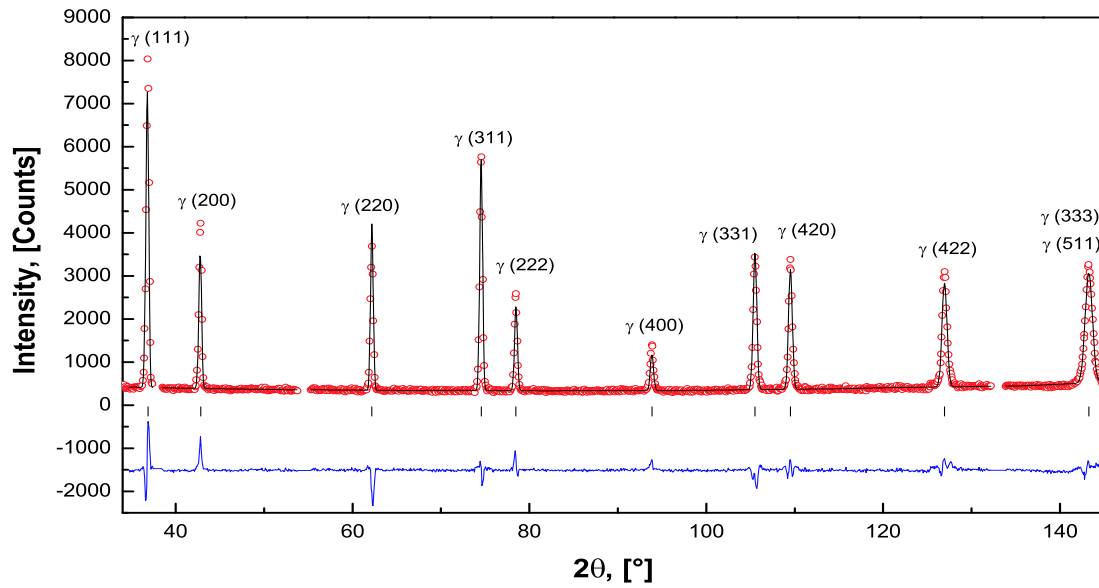


Figure 5.7: The Rietveld refinement of the powder neutron diffraction data of Fe-18Cr-10Ni (diffractometer E9, $\lambda=1.30747 \text{ \AA}$).

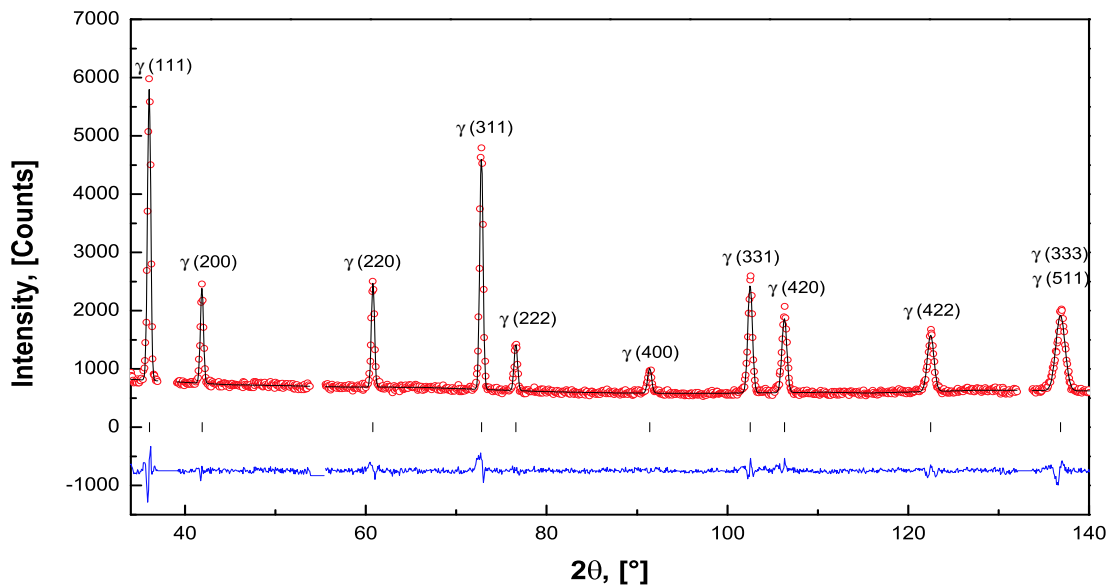


Figure 5.8: The Rietveld refinement of the powder neutron diffraction data of hydrogenated Fe-18Cr-10Ni with loading pressure of 2.3 GPa (diffractometer E9, $\lambda=1.30747 \text{ \AA}$).

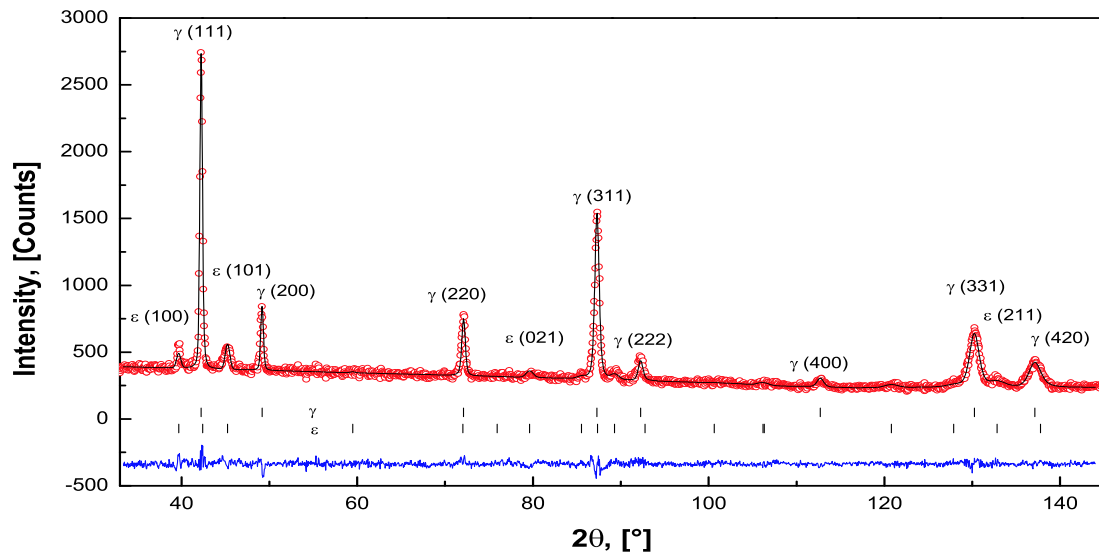


Figure 5.9: The Rietveld refinement of the powder neutron diffraction data of hydrogenated Fe-18Cr-10Ni with loading pressure of 3.0 GPa (diffractometer E9, $\lambda=1.30747$ Å).

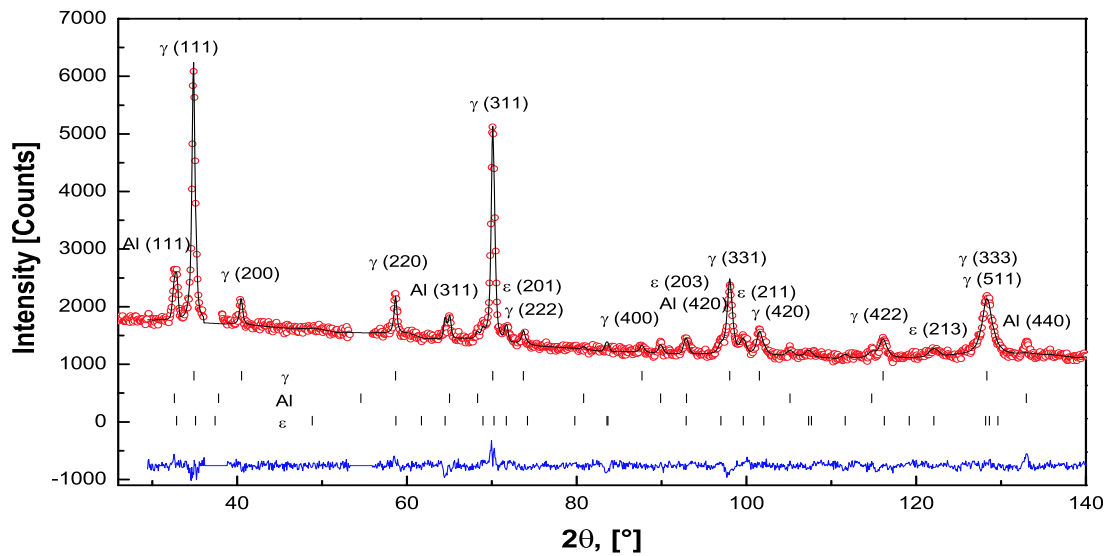


Figure 5.10: The Rietveld refinement of the powder neutron diffraction data of hydrogenated Fe-18Cr-10Ni with loading pressure of 7.0 GPa (diffractometer E9, $\lambda=1.30747$ Å).

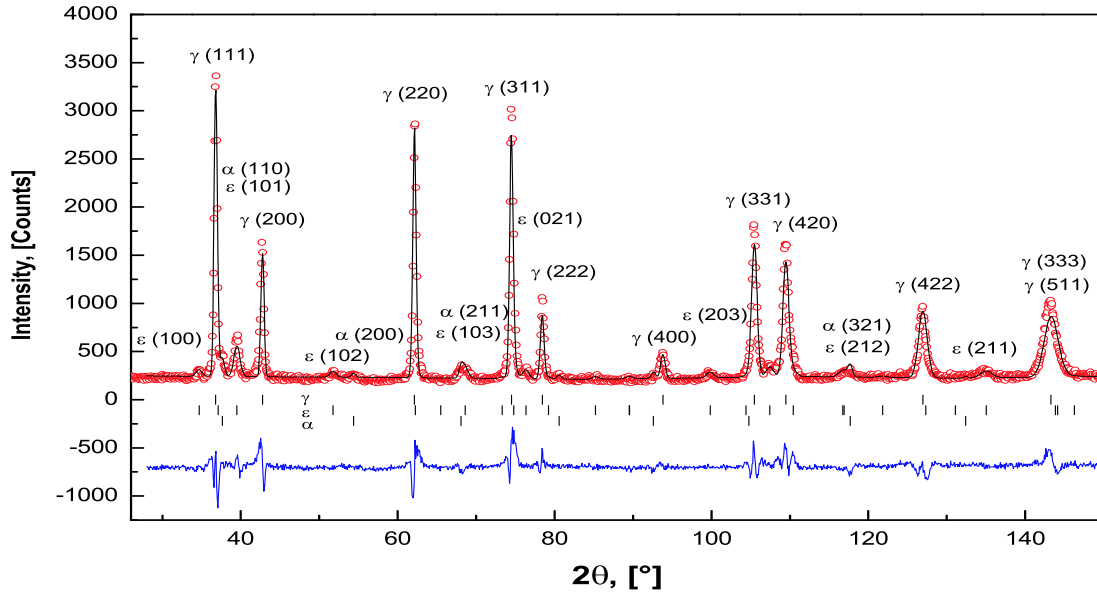


Figure 5.11: The Rietveld refinement of the powder neutron diffraction data of Fe-18Cr-10Ni pressure of 4.0 GPa (diffractometer E9, $\lambda=1.30747 \text{ \AA}$).

Table 5.2: Result of Rietveld refinement for austenitic stainless steel Fe-18Cr-10Ni

| hydrogenation pressure [GPa] | weight frac. of phases | lattice constant (at 80 K) | H occ. in octahed. sites | $B_{iso}(H)$ (\AA^2) |
|------------------------------|------------------------|-----------------------------------------------------|--------------------------|---------------------------------|
| uncharged | 100 % $Fm\bar{3}m$ | $a = 3.5800(1)$ | - | - |
| 2.3 | 100 % $Fm\bar{3}m$ | $a = 3.6537(1)$ | 30(2) % | 1.39 |
| 3.0 | 84 % $Fm\bar{3}m$ | $a = 3.6988(2)$ | 71(9)% | 1.41 |
| | 16 % $P6_3/mmc$ | $a = 2.617(2)$ $c = 4.254(3)$ $c/a = 1.626$ | | |
| 7.0 | $Fm\bar{3}m$ | $a = 3.7757(3)$ | 103(9) % | 1.48 |
| | $P6_3/mmc$ | $a = 2.6676(8);$ $c = 4.335(2)$ $c/a = 1.625$ | | |
| 4.0 without H | 86 % $Fm\bar{3}m$ | $a = 3.5785(2)$ | - | - |
| | 11 % $P6_3/mmc$ | $a = 2.6676(8);$ $c = 4.335(2)$ $c/a = 1.625$ | | |
| | 3 % $Im\bar{3}m$ | $a = 2.857(3)$ | | |

Simulation are performed to justify the results of Rietveld analysis in hydrogenated austenitic stainless steels. In the fcc structure exist two possible sites for hydrogen atoms: in tetrahedral and octahedral voids. Using the relation for F_{hkl} (eq. 3.7) it is easy to obtain relative intensity of the diffraction maxima.

Table 5.3: Structure factors $|F_{hkl}|^2$ for hydrogen in tetrahedral and octahedral interstitial sites.

| | H-tetrahedral sites | | H-octahedral sites |
|--------------|----------------------|--------------------|--------------------|
| | ZnS structure | random alloy | NaCl structure |
| $h,k,l=2n+1$ | $16(b_{Me}^2+b_H^2)$ | $16b_{Me}^2$ | $16(b_{Me}-b_H)^2$ |
| $h+k+l=4n$ | $16(b_{Me}+b_H)^2$ | $16(b_{Me}+b_H)^2$ | $16(b_{Me}+b_H)^2$ |
| $h+k+l=4n+2$ | $16(b_{Me}-b_H)^2$ | $16(b_{Me}-b_H)^2$ | |

Using a Fullprof program it is possible to perform simulation of neutron diffraction pattern for hydrogen atoms located in octahedral and tetrahedral interstitial sites.

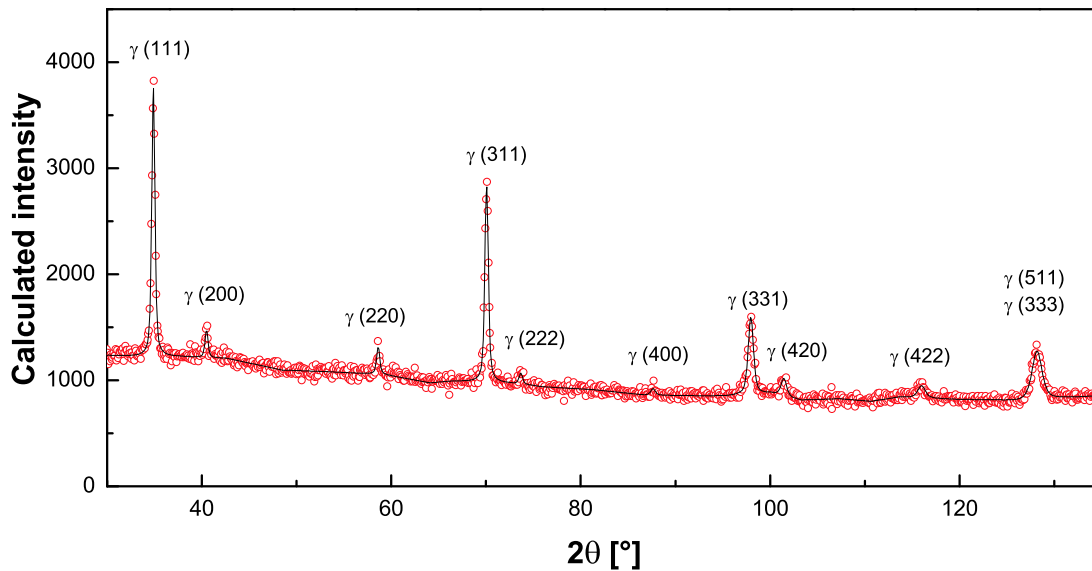


Figure 5.12: Simulated powder neutron diffraction pattern on Fe-25Cr-20Ni with hydrogen located in octahedral sites($H/Me=1$)

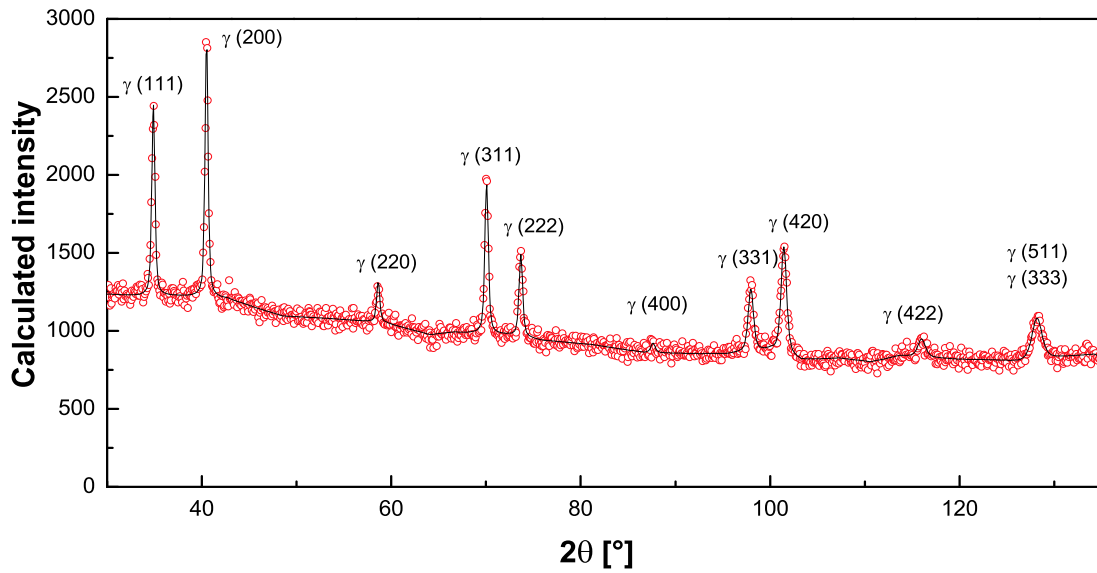


Figure 5.13: Simulated powder neutron diffraction pattern on Fe-25Cr-20Ni with hydrogen located in tetrahedral sites(H/Me=1)

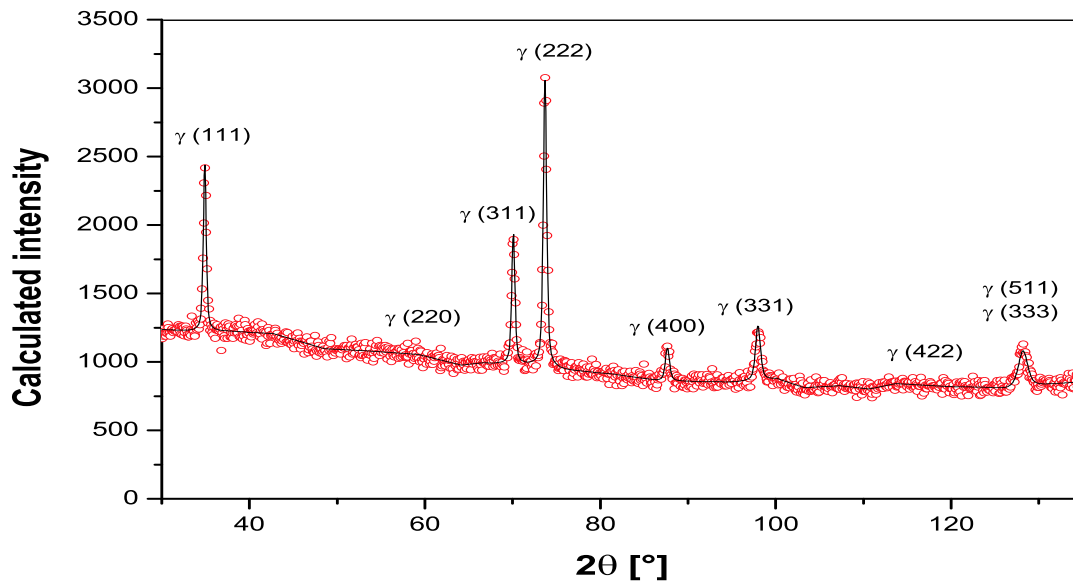


Figure 5.14: Simulated powder neutron diffraction pattern on Fe-25Cr-20Ni with hydrogen located in tetrahedral sites(H/Me=1) which build ZnS structure

5.1.3 Conclusion

From the result of Rietveld refinements for the austenitic stainless steels Fe-18Cr-10Ni and Fe-25Cr-20Ni it is straightforward to conclude about phase stability. Increase of the lattice parameter of both steels with increasing amount of hydrogen in interstitial sites. Austenitic stainless steel Fe-25Cr-20Ni(table 5.1) shows great stability on high pressure treatment up to 4.0 GPa as well as on the hydrogenation in high pressure cell. In the case of Fe-18Cr-10Ni(table 5.1.2) after hydrogenation under the pressure of 3.0(H/Me~0.56) and 7.0 GPa(H/Me~1) hexagonal phase appear. When only high pressure treatment(4.0 GPa) is applied appears not only hexagonal but also a minor fraction of body centered cubic(bcc) α -phase.

5.2 Inelastic neutron scattering

5.2.1 Experiment

Inelastic neutron scattering was performed on polycrystalline samples of hydrogenated austenitic stainless steels. In the phonon density of states $g(\omega)$ exist two modes: acoustic and optic with a gap between them.

Acoustic modes

Acoustic modes have energies similar to non-hydrogenated austenitic stainless steels which is in the range of 0-40 meV. Due to hydrogenation procedure strength of bonding and upper limit of acoustic modes are reduced. Inelastic neutron scattering was performed⁶ in FANS(Filter Analyser Neutron Spectrometer) at the National Institute of Standards and Technology(NIST) in Gaithersburg. This method also has significantly higher statistics. In the energy range of 20-25 meV a strong peak was observed. In this device Cu(220) is used as monochromator. In the case of neutrons which are nonrelativistic particles the further relation is valid:

$$\varepsilon = \frac{m_n v^2}{2} = \frac{h^2}{2m_n} \frac{1}{\lambda^2}. \quad (5.1)$$

The monochromated beam always contains $\lambda/2$ component. In the case of neutrons with energy of 25 meV the corresponding $\lambda/2$ component has an energy of 100 meV. Neutron which lost 25 meV could be scattered from acoustic or optic modes($\lambda/2$ component) of vibrations. In the experimental data strong overlapping of response of acoustic modes of the samples with excitation of optic modes occurs. This overlapping is so strong that it is impossible to distinguish between them.

⁶experiments were performed by Markus Hölzel

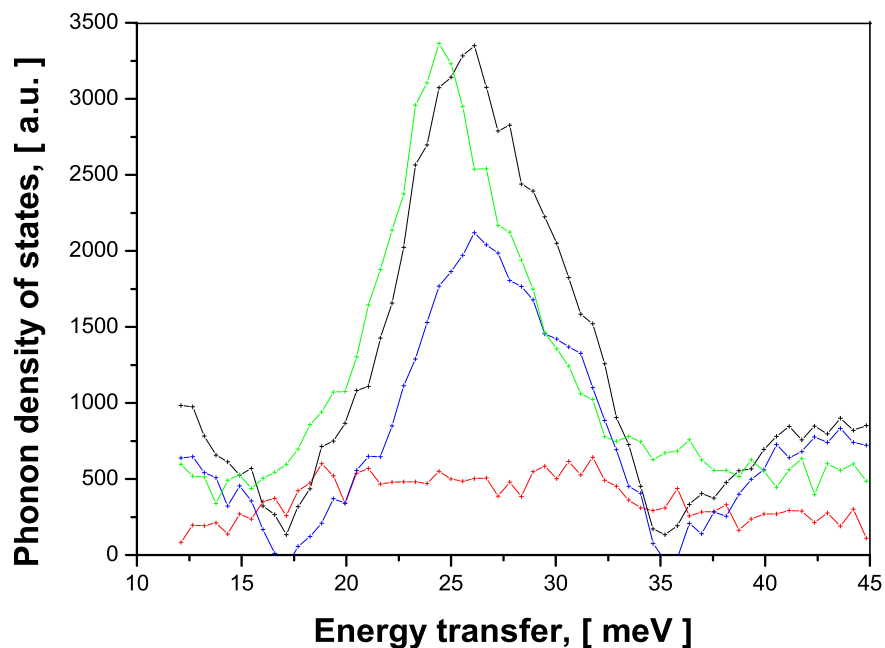


Figure 5.15: Experimental data for phonon density of states (---)austenitic stainless steel Fe-25Cr-20Ni without hydrogen, (---) Fe-25Cr-20Ni with H/Me=0.35(2), (---) Fe-18Cr-10Ni with H/Me=0.56(2) and (---) Fe-18Cr-10Ni with H/Me=1.03(9).

Optic modes

Vibration spectra of the hydrogen atoms are located in high energy region, over 100 meV. In this region $\hbar\omega \gg kT$ (eq. 3.38). Therefore energy loss spectroscopy is used which in this region has higher intensity. All spectrometers are optimised for high energy region and so the $\lambda/2$ component is reduced. INS was performed⁷ in FANS at NIST in Gaithersburg, IN1-BerF in the Institute Laue-Langevin (ILL) in Grenoble and TOF spectrometer TOSCA(Thermal Original Spectrometer with Cylindrical Analysers) in Rutherford Appleton Laboratory, Oxfordshire.

Filter spectrometers IN1-BerF and FANS measure neutron energy loss spectra with fixed final energy. Monochromatisation is performed by Bragg reflection on the monochromator crystal. In the case of IN1 spectrometer, neutrons came from the hot source with high flux. Spectrometer IN1-BerF has a beryllium filter which allows passing of neutrons with energy around 3.5 meV. FANS spectrometer use thermal neutrons and graphite and beryllium filters. The detection energy is fixed to value of a 1.8 meV.

Time of flight spectrometer TOSCA is mounted on the spallation source (ISIS) in the indirect geometry and as analyser graphite is used.

⁷experiments were performed by Markus Hölzel

5.2.2 Multiphonon correction

To obtain spectra for modelling, the multiphonon part has to be removed. On the spectra in the range 80-150 meV in multiphonon spectra exist one main contribution, which is a convolution of acoustic and optics modes. FANS spectrometer is optimised for data collection in the high energy range, so acoustics are or not measured at all or have big disturbance due to $\lambda/2$ contribution. Reliable data for acoustics not exist which are necessary for multiphonon correction.

The Debye-Waller exponent is proportional to differential cross section. Debye-Waller exponent is mainly determined through acoustic modes. Therefore values obtained from diffraction studies are used as starting values for the Debye-Waller exponent. Further refinement of Debye-Waller exponent was performed during multiphonon correction. With the assumption of similarity of acoustic modes of all austenitic stainless steels, density of states $g(\omega)$ was used as a base of the calculation. The obtained DOS for the austenitic stainless steels was corrected due to lattice expansion by Grüneisen parameter. On the corrected DOS for acoustic part of spectra its multiphonon contribution was superposed, in this case only first iteration. After that standard procedure for multiphonon correction was applied.

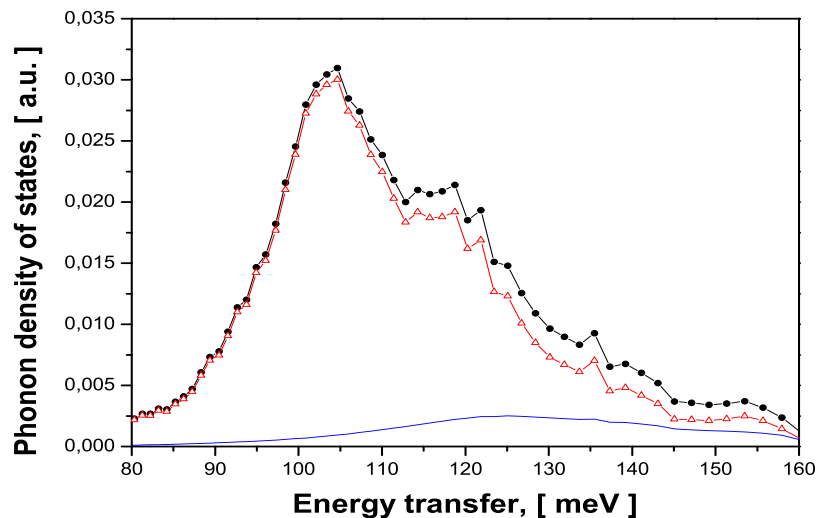


Figure 5.16: Optic modes in phonon density of states for hydrogenated austenitic stainless steel Fe-18Ni-10Cr(at 7.0 GPa) with H/Me=1.03(9), (-●-) experimental data, (—) multiphonon contribution and (-△-) DOS after multiphonon correction.

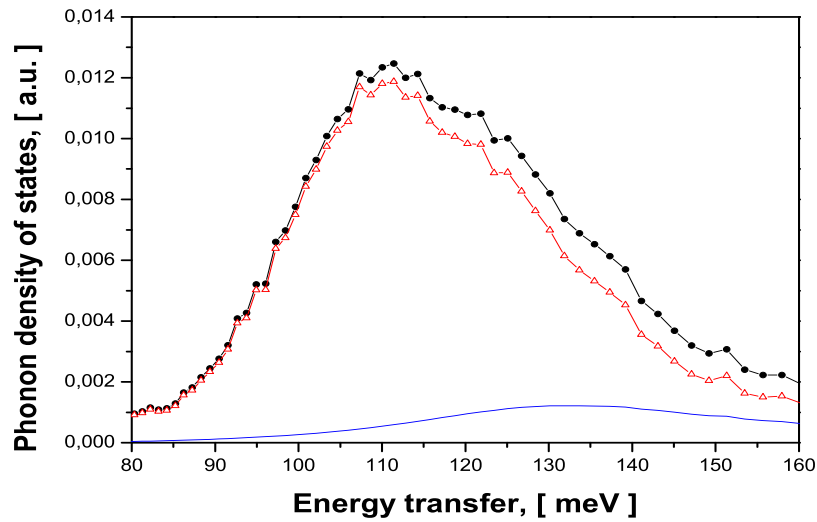


Figure 5.17: Optic modes in phonon density of states for hydrogenated austenitic stainless steel Fe-18Ni-10Cr(at 3.0 GPa) with H/Me=0.56(2), (●-) experimental data, (—) multiphonon contribution and (-△-) DOS after multiphonon correction.

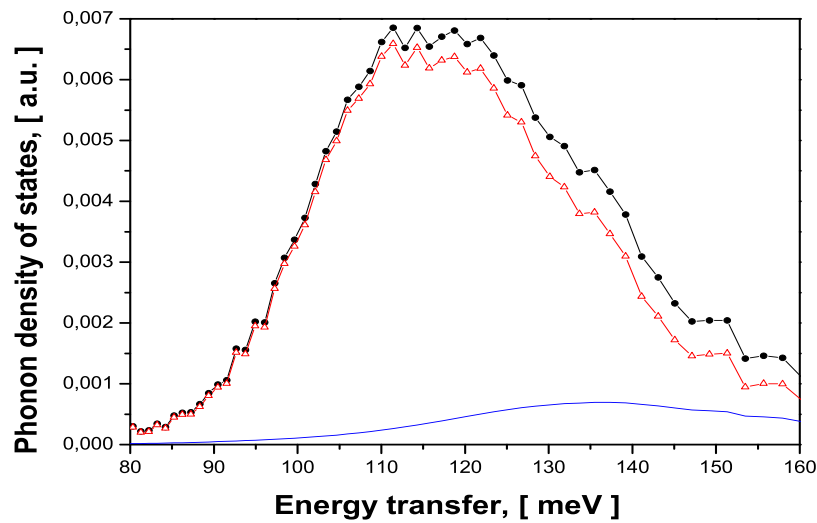


Figure 5.18: Optic modes in phonon density of states for hydrogenated austenitic stainless steel Fe-18Ni-10Cr(at 2.3 GPa) with H/Me=0.30(2), (●-) experimental data, (—) multiphonon contribution and (-△-) DOS after multiphonon correction.

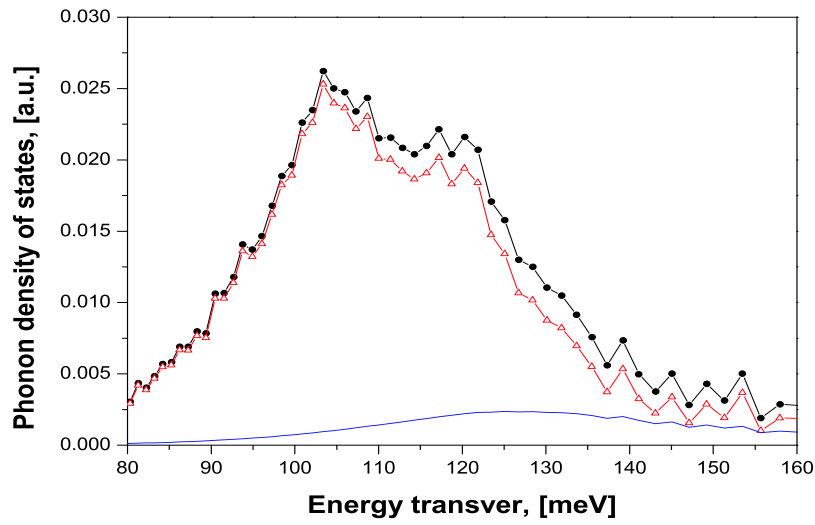


Figure 5.19: Optic modes in phonon density of states for hydrogenated austenitic stainless steel Fe-25Ni-20Cr(at 7.0 GPa) with H/Me=0.94(5), (●-) experimental data, (—) multi-phonon contribution and (-△-) DOS after multiphonon correction.

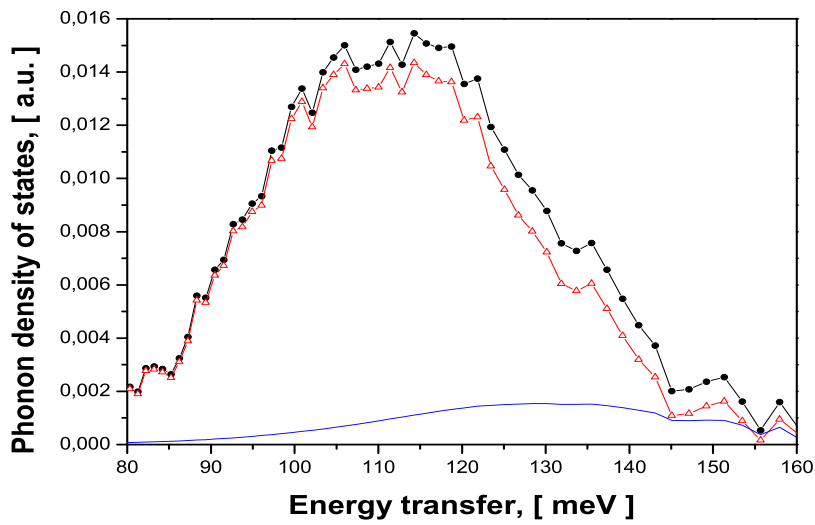


Figure 5.20: Optic modes in phonon density of states for hydrogenated austenitic stainless steel Fe-25Ni-20Cr(at 3.0 GPa) with H/Me=0.66(3), (●-) experimental data, (—) multi-phonon contribution and (-△-) DOS after multiphonon correction.